

# PhysDNet: Physics-Guided Decomposition Network of Side-Scan Sonar Imagery

Can Lei, Hayat Rajani, *Member, IEEE*, Nuno Gracias, Rafael Garcia, and Huigang Wang, *Member, IEEE*

**Abstract**—Side-scan sonar (SSS) has become an essential tool for seafloor mapping and underwater exploration. However, the measured intensity is entangled with seabed reflectivity, terrain elevation, and acoustic path loss, making the imagery highly view-dependent and hindering robust interpretation. To address this challenge, we propose PhysDNet, a physics-guided multi-branch network that explicitly decouples SSS images into three interpretable fields: reflectivity, elevation, and path loss. The network employs attention-augmented encoder–decoder branches, imposes range-wise consistency constraints on path loss, and incorporates a Lambertian-based reconstruction to enable progressive self-supervised training, thereby ensuring stable multi-task optimization while embedding physical priors into the learning process. Experiments demonstrate that the decomposed fields preserve geological structures, recover physically consistent illumination and attenuation, and enable accurate shadow prediction. These findings confirm that physics-guided decomposition establishes a stable and interpretable domain for SSS analysis, enhancing both physical consistency and downstream applications such as registration and shadow interpretation.

**Index Terms**—Side-scan sonar, Physics-guided decomposition, Multi-branch network, Self-supervised learning.

## I. INTRODUCTION

**S**IDE-scan sonar (SSS) is an essential tool for underwater remote sensing, widely used in seafloor mapping, ecological monitoring, and geological interpretation [1]. It provides large-scale backscatter imagery for detailed characterization of seabed morphology and texture. However, the measured intensity reflects a coupled effect of seabed reflectivity, terrain elevation, and acoustic path loss [2], making SSS imagery highly view-dependent and sensitive to acquisition geometry, which in turn reduces physical interpretability and the robustness of downstream tasks such as registration, shadow analysis, and target recognition.

Most existing approaches to SSS analysis operate directly on intensity images. For registration and target recognition, classical methods such as SIFT and AKAZE [3] and recent deep networks [4] have been applied to sonar data to extract features for consistent matching, but the strong view

dependence of SSS often makes them unstable across passes. Shadow analysis has similarly used geometry-based thresholding [5] and modern segmentation networks [6], which provide information for object height and occlusion, but their reliance on manual annotations and susceptibility to multipath scattering remain major challenges. As a result, existing methods struggle to obtain reliable features and shadow, highlighting the need to separate viewpoint-dependent effects from intrinsic seabed properties.

Recent studies have explored learning-based decomposition of SSS intensity. Huang et al. [7] proposed a DCNN to recover terrain, reflectivity, roughness, and beam pattern, demonstrating that physics-inspired maps can be learned without supervision, but modeling roughness as a single scalar limited interpretability and ignored its correlation with reflectivity. More recently, a diffusion-inspired U-Net with time embeddings and encoder-level attention was introduced to jointly predict terrain, reflectivity, and beam pattern, improving sediment classification [8], but unstable training from time embeddings and attention confined to the encoder reduced task-specific focus. Overall, these efforts highlight the promise of physics-guided learning but leave representations still partially entangled in the intensity domain, underscoring the need for a more explicit and stable decomposition.

In this paper, we present PhysDNet, a physics-guided multi-branch network that explicitly decomposes SSS imagery into three interpretable fields: seabed reflectivity, terrain elevation, and acoustic path loss. Compared with prior approaches, PhysDNet introduces three key contributions:

- Explicit three-branch architecture that embeds roughness variability within the reflectivity map and enforces range-wise consistency in path loss, ensuring physically meaningful outputs;
- Attention-augmented encoder–decoders that integrate channel attention across modules, attention gates in skip connections, and coordinate attention in the bottleneck, thereby strengthening task-specific feature learning;
- Progressive self-supervised training strategy that sequentially emphasizes different physical components, stabilizing convergence and improving generalization across environments.

## II. METHOD

SSS intensity is strongly view-dependent due to anisotropic backscattering and shadowing, whereas seafloor structures (edges, contours, major geological formations) remain relatively stable across passes. Inspired by a Lambertian-like factorization for seabed imaging [7], we decompose SSS into

Can Lei and Huigang Wang are with the School of Marine Science and Technology, Northwestern Polytechnical University, Xi’an 710072, China. Huigang Wang is also with the Research & Development Institute of Northwestern Polytechnical University in Shenzhen, Shenzhen 518057, China.

Hayat Rajani, Nuno Gracias and Rafael Garcia are with the Computer Vision and Robotics Research Institute (ViCOROB) of the University of Girona, Spain. This work was conducted while Can Lei was on a research stay at ViCOROB, Spain

This work was partly supported by the Spanish government through projects ASSiST (PID2023-149413OB-I00) and IURBI (CNS2023-144688). This work was also supported by the National Natural Science Foundation of China (62171368) and Science, Technology and Innovation of Shenzhen Municipality (JCYJ20241202124931042).

Corresponding author: Huigang Wang (e-mail: wanghg74@nwpu.edu.cn).

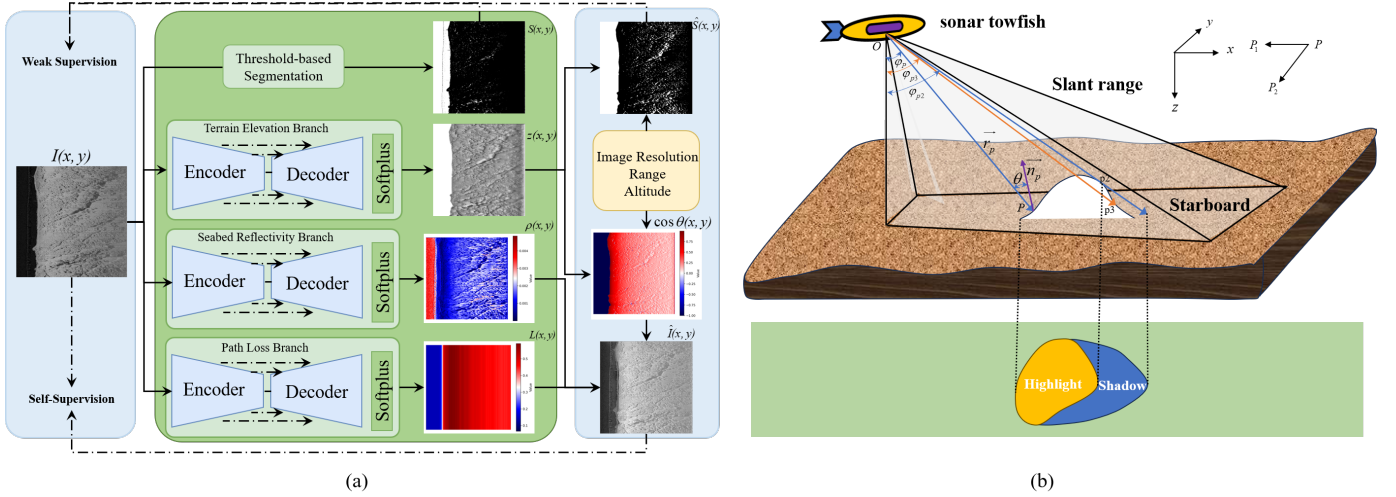


Fig. 1. Overview of the proposed PhysDNet framework and the geometric definitions used in the physics-aware model. (a) PhysDNet employs a three-branch architecture to decouple SSS images into reflectivity ( $\rho$ ), terrain elevation ( $z$ ), and path loss ( $L$ ), guided by the Lambertian model. A threshold-based shadow map  $S(x, y)$  provides weak supervision, while predicted elevation supports physical computation of  $\cos \theta$  and a physics-driven shadow map  $\hat{S}(x, y)$ . (b) At ping index  $i$ , the transducer at  $O = (0, y_i, 0)$  emits toward seafloor points  $P(x_{ij}, y_i, z_{ij})$ . The reflection angle  $\theta$  is defined between the acoustic incidence vector  $\vec{OP}$  and the local surface normal (from neighbors  $P_1, P_2$ ). The propagation angle  $\varphi$  measures the grazing angle relative to the vertical axis. Points  $P, p_2$ , and  $p_3$  illustrate the angular monotonicity rule for shadow detection, where  $p_3$  lies in the acoustic shadow.

three physically interpretable fields (Fig. 1(a)): (i) seabed reflectivity  $\rho$  (viewpoint-stable substrate property), (ii) the incidence factor  $\cos \theta$  parameterized by terrain elevation  $z$ , and (iii) the propagation path-loss  $L$ . We propose PhysDNet, a multi-branch encoder–decoder that jointly predicts  $\rho, z$ , and  $L$  from a single SSS image, thereby enabling this decomposition.

### A. Multi-branch Physical Decoupling Network Architecture

PhysDNet comprises three parallel branches with identical topology and independent parameters. Each branch takes the SSS intensity as input and outputs one physical map— $\rho, z$ , and  $L$ —enabling explicit decomposition. Because  $L$  varies predominantly with range, we enforce range-wise consistency by averaging the predicted  $L$  along columns and vertically replicating the result to a 2D field.

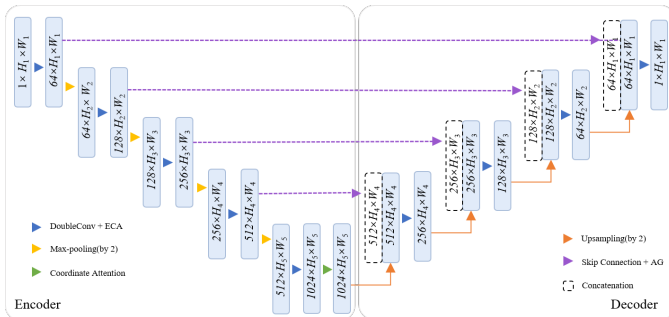


Fig. 2. Schematic of a single encoder–decoder branch in PhysDNet. The design includes ECA (Efficient Channel Attention) in all convolution blocks, AG (Attention Gates) for refining skip connections, Coordinate Attention in the bottleneck, and an OutConv + Softplus for non-negative outputs.

Each branch adopts an attention-augmented encoder–decoder structure consisting of an initial DoubleConv + ECA (Efficient Channel Attention),

four encoder stages (MaxPool + DoubleConv + ECA), and a symmetric decoder with four upsampling stages connected by skip links. To enhance feature representation, ECA is appended to every DoubleConv block. All skip connections are refined by AG (Attention Gates) before concatenation, while the bottleneck incorporates Coordinate Attention to capture long-range, direction-aware dependencies. Finally, a OutConv followed by Softplus ensures non-negativity. This design preserves the hierarchical representation capacity of the encoder–decoder while incorporating ECA for lightweight channel attention and AG for skip-wise spatial gating, emphasizing physically critical regions and laying the foundation for the physics-guided self-supervised learning introduced later (Fig. 2).

### B. Reflection Angle Calculation and Intensity Reconstruction

To reconstruct the sonar intensity image  $\hat{I}(x, y)$  from the network outputs of terrain elevation  $z(x, y)$ , seabed reflectivity  $\rho(x, y)$ , and propagation loss  $L(x, y)$ , it is necessary to incorporate the reflection angle  $\theta(x, y)$ . According to the Lambertian reflection model [8], the acoustic intensity is proportional to the cosine of the angle between the incident direction and the local seabed normal, formulated as:

$$\hat{I}(x, y) = \rho(x, y) \cdot \cos \theta(x, y) \cdot L(x, y) \quad (1)$$

Accurately computing  $\cos \theta(x, y)$  for each pixel is thus essential for reconstructing sonar intensity and supervising the network via physically grounded loss functions.

1) *Spatial Coordinate System Definition*: As illustrated in Fig. 1(b), we define a 3D spatial coordinate system to model acoustic propagation, where the x-axis aligns with the sonar range direction, the y-axis follows the along-track direction (ping index), and the z-axis points downward. The origin  $O = (0, 0, 0)$  is set at the transducer position at the start of scanning.

At ping  $i$ , the transducer is located at  $(0, y_i, 0)$ , where  $y_i = i \cdot \Delta y$  and  $\Delta y$  is the fixed ping interval. The  $j$ -th pixel at ping  $i$  corresponds to a seafloor point  $P = (x_{ij}, y_i, z_{ij})$ , where  $z_{ij}$  is the predicted seabed elevation. Since the SSS image stores slant range  $r_{ij}$  along the image  $x$ -axis, the lateral coordinate is recovered by:  $x_{ij} = \sqrt{r_{ij}^2 - z_{ij}^2}$ , ensuring subsequent geometry is consistent in 3D.

2) *Cosine of the Reflection Angle*: The incidence vector from the source to  $P$  is  $\vec{r}_p = \vec{OP} = (x_{ij}, 0, z_{ij})$ . The local surface normal  $\vec{n}_p$  is estimated from a tangent plane spanned by the left and previous-ping neighbors  $P_1 = (x_{i,j-1}, y_i, z_{i,j-1})$  and  $P_2 = (x_{ij}, y_{i-1}, z_{i-1,j})$ . The tangent vectors are

$$\begin{aligned} \vec{v}_1 &= \vec{P_1P} = (x_{ij} - x_{i,j-1}, 0, z_{ij} - z_{i,j-1}) \\ \vec{v}_2 &= \vec{P_2P} = (0, y_i - y_{i-1}, z_{ij} - z_{i-1,j}) \end{aligned} \quad (2)$$

and  $\vec{n}_p = \vec{v}_1 \times \vec{v}_2$ . Finally, the cosine of the reflection angle is calculated via the normalized dot product:

$$\cos \theta_p = \frac{\vec{r}_p \cdot \vec{n}_p}{\|\vec{r}_p\| \cdot \|\vec{n}_p\|} \quad (3)$$

3) *Intensity Reconstruction*: The reconstructed map  $\hat{I}(x, y)$  provides intermediate supervision by direct comparison to the raw SSS  $I(x, y)$ , guiding the network to learn seafloor geometry (via  $\cos \theta$ ) and acoustic backscatter (via  $\rho$ ) under physically consistent propagation ( $L$ ).

### C. Shadow Map Generation

Acoustic shadows, defined as regions occluded from the sonar line of sight, encode strong constraints on seafloor relief. We derive a shadow map from the predicted elevation  $z$  and use it as weak supervision to regularize  $z$  in the absence of ground-truth heights.

1) *Propagation Angle*: Given the predicted elevation map  $z(x, y)$  (with  $z > 0$  representing seafloor depth), the 3D coordinate of a pixel at row  $i$  (ping index) and column  $j$  (range index) is defined as  $P = (x_{ij}, y_i, z_{ij})$ . We define the propagation angle  $\varphi_{ij}$  between the acoustic ray from the transducer to the point  $P$  and the vertical  $z$ -axis:

$$\tan \varphi_{ij} = \frac{x_{ij}}{z_{ij}}, \quad \varphi_{ij} = \arctan \left( \frac{x_{ij}}{z_{ij}} \right) \quad (4)$$

2) *Shadow Detection via Angle Monotonicity*: Along each ping (fixed  $i$ ), visibility must follow the nondecreasing envelope of  $\varphi_{ij}$ ; terrain that raises the envelope occludes subsequent points with smaller grazing angles. We therefore classify  $(i, j)$  as shadowed if:

$$\varphi_{ij} < \max_{k < j} \varphi_{ik} \quad (5)$$

This one-pass near-to-far scan per ping efficiently yields the shadow mask  $\hat{S}(x, y)$  from  $z(x, y)$ . To illustrate this, Fig. 1(b) shows three sequential points  $P$ ,  $p_2$ , and  $p_3$  with  $\varphi_P < \varphi_{p_3} < \varphi_{p_2}$ . Here,  $p_2$  is the last visible point before occlusion, while  $p_3$ , falling behind a steeper slope, is correctly identified as being in shadow.

### D. Loss Function Design and Training Strategy

The proposed physically decoupled network adopts a multi-branch, multi-task architecture to jointly estimate the seafloor elevation map  $z(x, y)$ , bottom reflectivity  $\rho(x, y)$ , and acoustic path loss  $L(x, y)$ . In the absence of ground truth annotations for these physical quantities, we develop a three-stage training strategy, guided by sonar imaging physics and weak supervision signals.

1) *Stage 1: Initial Terrain Fitting and Row-wise Smoothness*: This stage aims to learn the coarse structure of the seafloor elevation. A weak reference elevation map  $z_{\text{ref}}(x, y)$  is constructed by propagating the estimated bottom height from each ping, derived directly from the raw sensor data (e.g., altitude measurements). This reference serves as an initial terrain prior to guide the prediction of  $z(x, y)$ . The training loss combines an elevation fitting term  $\mathcal{L}_{z\_fit}$  and a smoothness regularization  $\mathcal{L}_{z\_row}$ :

$$\begin{aligned} \mathcal{L}_{\text{stage1}} &= \mathcal{L}_{z\_fit} + \mathcal{L}_{z\_row} \\ \mathcal{L}_{z\_fit} &= \|z(x, y) - z_{\text{ref}}(x, y)\|_1 \\ \mathcal{L}_{z\_row} &= \sum_y \sum_x |z(x+1, y) - z(x, y)| \end{aligned} \quad (6)$$

The term  $\mathcal{L}_{z\_row}$  encourages local continuity of the estimated elevation along the range ( $x$ ) direction, consistent with the physical continuity of seafloor topography and the scanning geometry of side-scan sonar.

2) *Stage 2: Terrain Refinement with Shadow-guided Structural Consistency*: Building upon the coarse terrain estimated in Stage 1, this stage introduces vertical consistency, acoustic image fidelity, and weak supervision from shadow patterns. The overall loss integrates column-wise smoothness  $\mathcal{L}_{z\_col}$ , SSIM-based reconstruction  $\mathcal{L}_{ssim}$ , and shadow guidance  $\mathcal{L}_{shd}$ :

$$\begin{aligned} \mathcal{L}_{\text{stage2}} &= \mathcal{L}_{z\_col} + \mathcal{L}_{ssim} + \mathcal{L}_{shd} \\ \mathcal{L}_{z\_col} &= \sum_x \sum_y |z(x, y+1) - z(x, y)| \\ \mathcal{L}_{ssim} &= 1 - \text{SSIM}(I(x, y), \hat{I}(x, y)) \\ \mathcal{L}_{shd} &= \|S(x, y) - \hat{S}(x, y)\|_1 \end{aligned} \quad (7)$$

Analogous to  $\mathcal{L}_{z\_row}$ ,  $\mathcal{L}_{z\_col}$  enforces vertical ( $y$ ) smoothness of  $z$ , promoting cross-ping structural consistency. The SSIM term  $\mathcal{L}_{ssim}$  drives the reconstruction  $\hat{I}$  to preserve the structural characteristics of the original SSS image  $I$ . The shadow-trend loss  $\mathcal{L}_{shd}$  provides weak supervision by comparing the predicted shadow map  $\hat{S}$  with a coarse, thresholded mask  $S$  from raw SSS; rather than enforcing pixel-level alignment, it encourages learning terrain structures that cause acoustic occlusions. Because shadows arise from elevation variations,  $S$  indirectly refines  $z$ , and improved  $z$  increases the reliability of the reflectivity and path-loss maps, which lack direct supervision.

3) *Stage 3: Joint Optimization and Semantic Enhancement*: This stage integrates all branches and promotes semantically meaningful reconstruction. The loss includes Elevation Smoothness Loss  $\mathcal{L}_{z\_smt}$ , Perceptual Loss  $\mathcal{L}_{perc}$ , Shadow Loss  $\mathcal{L}_{shd}$ , Path Loss Constraint  $\mathcal{L}_{pth}$ , Reflectivity Smoothness Loss  $\mathcal{L}_{\rho\_smt}$ , and combined loss  $\mathcal{L}_{\text{stage3}}$ :

$$\begin{aligned}
\mathcal{L}_{stage3} &= \mathcal{L}_{z\_smt} + \mathcal{L}_{perc} + \mathcal{L}_{shd} + \mathcal{L}_{pth} + \mathcal{L}_{\rho\_smt} \\
\mathcal{L}_{z\_smt} &= \mathcal{L}_{z\_row} + \mathcal{L}_{z\_col} \\
\mathcal{L}_{perc} &= \|\Phi(I) - \Phi(\hat{I})\|_2^2 \\
\mathcal{L}_{pth} &= \|\text{mean}_y(L(x, y)) - \bar{I}(x)\|_1 \\
\mathcal{L}_{\rho\_smt} &= \sum_{x,y} |\rho(x+1, y) - \rho(x, y)| + |\rho(x, y+1) - \rho(x, y)|
\end{aligned} \tag{8}$$

here,  $\Phi$  extracts features from the first 10 layers of a pretrained MobileNetV3, so  $\mathcal{L}_{perc}$  encourages learning deep semantic patterns.  $\bar{I}(x)$  is the column-wise mean intensity of  $I$ , used to fit the predicted path-loss  $L(x, y)$ ; thus  $\mathcal{L}_{pth}$  enforces consistency with actual (range-dependent) acoustic attenuation.  $\mathcal{L}_{\rho\_smt}$  regularizes spatial smoothness of  $\rho$  to avoid spurious jumps, and  $\mathcal{L}_{z\_smt}$  preserves terrain continuity. This staged training progressively learns terrain, enforces physical constraints, and injects semantic guidance; even without ground truth, the model leverages image structure, physical priors, and weak supervision to yield disentangled predictions of  $z$ ,  $\rho$ , and  $L$ .

### III. EXPERIMENT

#### A. Data Description

1) *Data Acquisition and Preprocessing*: We use SSS data from sector N07 of [9], acquired with a Klein 3000H at 500 kHz; ranges were adjusted between 50 m and 100 m by bathymetry, with altitude 10% of range, yielding an average slant-range resolution of 8.5 cm. The raw .xtf files provide intensities and metadata (altitude, range, USBL, heading). Pre-processing includes log-intensity normalization, port/starboard separation with port flipped, stacking pings into 2D waterfalls, and tiling into 1024×1024 patches with synchronized metadata for geometric modeling. The dataset is divided into 6734 training, 1704 validation, and 122 test samples, with the test set from regions distinct from the training and validation data.

#### B. Experimental settings

Experiments were run on Ubuntu with Python/PyTorch on a workstation with dual Intel® Xeon® Gold 6230 CPUs, 376 GB RAM, and two NVIDIA Quadro RTX 6000 GPUs (CUDA 12.0, driver 525.147.05). Models were trained for 200 epochs (batch size 16) using Adam (lr=1 × 10<sup>-3</sup>, β = (0.9, 0.999), weight decay=5 × 10<sup>-4</sup>) with a cosine-annealing schedule and 30-epoch warmup, decaying the learning rate to 1 × 10<sup>-6</sup>. Training follows a three-stage curriculum (epochs 0–60, 60–120, 120–200). Mixed precision, cuDNN acceleration, and gradient clipping are used for efficiency and stability.

#### C. Experimental Results

1) *Physical Decomposition Results*: As shown in Fig. 3 and Table I, the reconstructed intensity maps closely approximate the original SSS, reproducing the spatial backscatter distribution ( $S=0.83$ ,  $M=0.04$ ,  $P=0.02$ ). The reflectivity maps suppress view-dependent fluctuations while preserving stable geological structures, confirming the viewpoint-invariant property of  $\rho$ . The cosine maps capture illumination variation, and the path-loss maps show the expected monotonic attenuation with range, with strong spatial coherence and low error

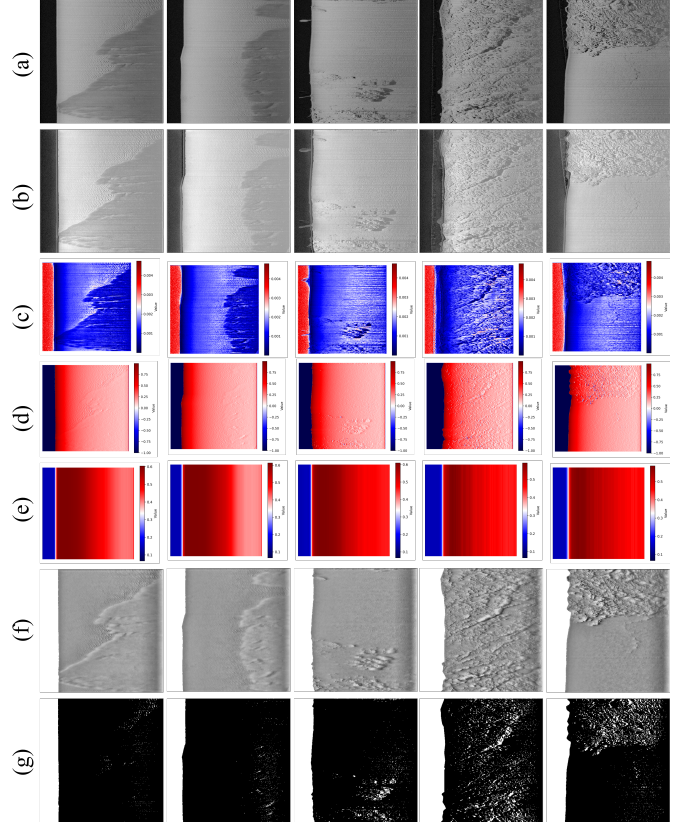


Fig. 3. Visualization of the outputs from the multi-branch physically decoupled network. Each column corresponds to a test case, with 5 cases in total. From top to bottom: (a) raw side-scan sonar image; (b) predicted acoustic intensity map; (c) predicted seabed reflectivity map; (d) predicted cosine of the reflection angle ( $\cos \theta$ ); (e) predicted acoustic path loss map; (f) predicted seabed elevation map (converted from depth); (g) shadow mask inferred from the predicted elevation.

TABLE I  
QUANTITATIVE RESULTS OF OUR METHOD USING METRIC VARIABLES.

**Note**:  $S$  denotes structural similarity between  $\hat{I}(x, y)$  and  $I(x, y)$ ;  $M$  denotes mean squared error;  $P$  denotes perceptual error.  $\bar{e}_z$  denotes mean absolute error of elevation;  $\sigma_z$  denotes standard deviation of the error.  $\bar{e}_L$  denotes mean absolute error of path-loss;  $\sigma_L$  denotes standard deviation of the error.

$S$	$M$	$P$	$\bar{e}_z$	$\sigma_z$	$\bar{e}_L$	$\sigma_L$	Params	FPS
0.83	0.04	0.02	0.32	0.07	0.007	0.004	55.2M	30

( $\bar{e}_L=0.007$ ,  $\sigma_L=0.004$ ). The elevation maps follow seafloor undulations and interpolate smoothly across shadows, yielding bounded error ( $\bar{e}_z=0.32$  m,  $\sigma_z=0.07$  m). In addition, terrain underestimation derived from  $z$  delineates shadow onsets and transitions, producing masks with cleaner boundaries and fewer omissions than heuristic thresholding.

2) *Shadow-Based Evaluation*: Since no public ground truth exists for  $z$ ,  $\rho$ , and  $L$ , we validate the decomposition in the shadow domain, where shadows are derived from predicted  $z$  through imaging geometry. We compare against adaptive thresholding [5] and five representative segmentation baselines, including OCRNet [10], BiSeNet [11], Mask2Former [12], and SegFormer [13]. All deep baselines are trained on the

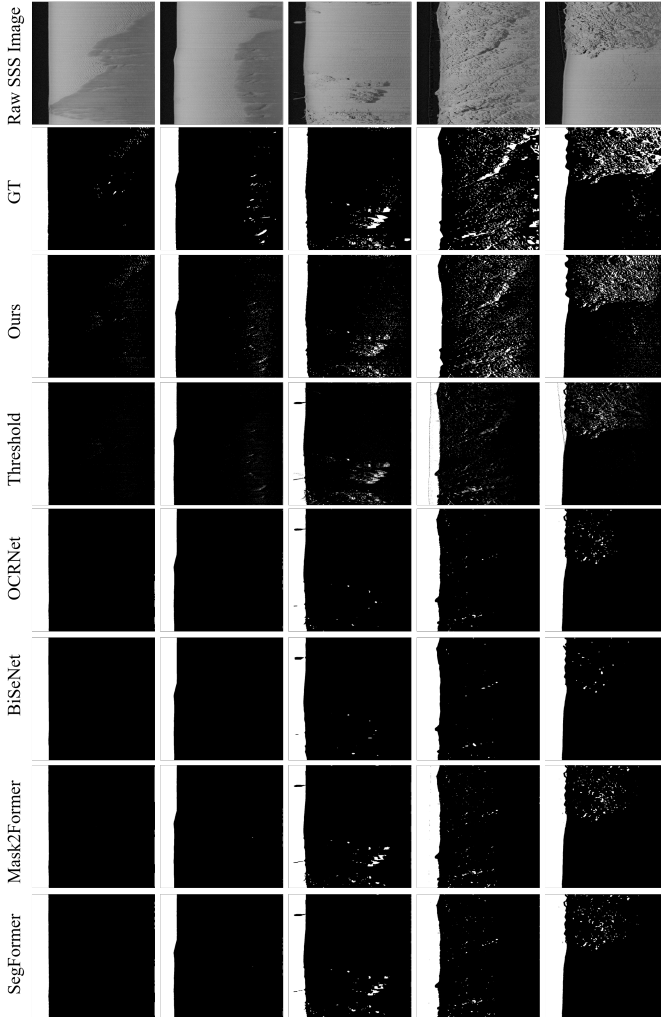


Fig. 4. Shadow segmentation comparison. From top to bottom, input SSS, manual GT, ours (shadows derived from predicted  $z$ ), adaptive threshold, OCRNet, BiSeNet, Mask2Former, SegFormer. Our method best matches GT and recovers fine-scale shadow regions.

TABLE II

SHADOW SEGMENTATION COMPARISON PERFORMANCE ON THE TEST SET.

**Note:** IoU denotes intersection over union; ACC denotes pixel accuracy; P denotes precision; R denotes recall.

Method	IoU	ACC	P	R
Threshold [5]	77.6%	89.17%	87.99%	78.74%
OCRNet [10]	75.89%	87.99%	86.67%	76.02%
BiSeNet [11]	75.84%	87.92%	86.60%	75.86%
Mask2Former [12]	77.15%	88.66%	87.37%	77.41%
SegFormer [13]	77.06%	88.61%	87.29%	77.29%
<b>Ours</b>	<b>92.64%</b>	<b>96.97%</b>	<b>96.40%</b>	<b>94.49%</b>

same threshold-generated masks, and performance is evaluated on a manually annotated test set using IoU, ACC (Accuracy), P (Precision), and R (Recall).

As shown in Fig. 4 and Table II, our method best matches ground truth, recovering fine-scale and low-contrast shadows that other methods consistently miss. SegFormer and Mask2Former perform best among the baselines but still fail

on small shadow structures, while others capture only coarse blobs. Quantitatively, our method achieves IoU 92.64%, ACC 96.97%, Precision 96.40%, and Recall 94.49%, with the most notable gain in recall (+17.1% over the best deep baseline), reflecting its superior recovery of small and subtle shadows.

#### IV. CONCLUSION

In this paper, we introduced PhysDNet, a physics-guided multi-branch network that disentangles SSS imagery into seabed reflectivity, terrain elevation, and acoustic path loss. By combining acoustic imaging physics with attention mechanisms and progressive self-supervised training, the framework provides interpretable representations that enhance robustness in downstream analysis. Experiments demonstrated consistent decompositions, where reflectivity maps preserve viewpoint-invariant structures, elevation maps provide reliable shadow cues, and path-loss maps follow expected attenuation trends. However, the current framework is limited by its reliance on a Lambertian reflection approximation, which simplifies acoustic scattering and may reduce accuracy under complex seabed conditions. Future work will focus on incorporating more advanced scattering models to enhance physical fidelity while maintaining interpretability.

#### REFERENCES

- [1] H. P. Johnson and M. Helferty, "The geological interpretation of side-scan sonar," *Reviews of Geophysics*, vol. 28, no. 4, pp. 357–380, 1990.
- [2] A. Burguera and G. Oliver, "High-resolution underwater mapping using side-scan sonar," *PLoS One*, vol. 11, no. 1, p. e0146396, 2016.
- [3] Z. Wang, J. Li, X. Wang, and X. Niu, "Underwater terrain image stitching based on spatial gradient feature block," *Computers, Materials & Continua*, vol. 72, no. 2, 2022.
- [4] C. Lei, H. Wang, and J. Lei, "Si-gat: Enhancing side-scan sonar image classification based on graph structure," *IEEE Sensors Journal*, vol. 24, no. 15, pp. 24 388–24 404, 2024.
- [5] M. Zhang, W. Cai, Y. Wang, and J. Zhu, "A level set method with heterogeneity filter for side-scan sonar image segmentation," *IEEE Sensors Journal*, vol. 24, no. 1, pp. 584–595, 2023.
- [6] H. Rajani, N. Gracias, and R. Garcia, "A convolutional vision transformer for semantic segmentation of side-scan sonar data," *Ocean Engineering*, vol. 286, p. 115647, 2023.
- [7] C. Huang, H. Zhang, J. Zhao, Y. Yu, and X. Zhao, "Unsupervised terrain reconstruction from side scan sonar constrained to the imaging mechanism," *IEEE Transactions on Geoscience and Remote Sensing*, 2024.
- [8] C. Huang, J. Zhao, and H. Zhang, "Classification and analysis of seafloor sediments using hidden features from combined imaging mechanism and seafloor reflection model," *IEEE Transactions on Geoscience and Remote Sensing*, 2024.
- [9] H. Rajani, V. Franchi, B. M.-C. Valles, R. Ramos, R. Garcia, and N. Gracias, "Benthicat: An opti-acoustic dataset for advancing benthic classification and habitat mapping," 2025. [Online]. Available: <https://arxiv.org/abs/2510.04876>
- [10] Y. Yuan, X. Chen, and J. Wang, "Object-contextual representations for semantic segmentation," in *European Conference on Computer Vision*. Springer, 2020, pp. 173–190.
- [11] C. Yu, C. Gao, J. Wang, G. Yu, C. Shen, and N. Sang, "Bisenet v2: Bilateral network with guided aggregation for real-time semantic segmentation," *International Journal of Computer Vision*, vol. 129, no. 11, pp. 3051–3068, 2021.
- [12] B. Cheng, I. Misra, A. G. Schwing, A. Kirillov, and R. Girdhar, "Masked-attention mask transformer for universal image segmentation," in *Proceedings of the IEEE/CVF Conference on Computer Vision and Pattern Recognition*, 2022, pp. 1290–1299.
- [13] H. Bai, P. Wang, R. Zhang, and Z. Su, "Segformer: A topic segmentation model with controllable range of attention," in *Proceedings of the AAAI Conference on Artificial Intelligence*, vol. 37, no. 11, 2023, pp. 12 545–12 552.